Preliminary Experimental Evidence of Anisotropy of Turbulence at Maui Space Surveillance Site

Mikhail S. Belen'kii
Trex Enterprises Corporation
10455 Pacific Center Court San Diego, CA 92121
Edward Cuellar
Trex Enterprises Corporation
2701 Pan American Freeway NE, Suite C, Albuquerque, NM 87107
Kevin A. Hughes
Trex Enterprises Corporation
10455 Pacific Center Court San Diego, CA 92121
Vincent A. Rye
Trex Enterprises Corporation
10455 Pacific Center Court San Diego, CA 92121

ABSTRACT

We investigated the spatial structure of atmospheric turbulence at Maui Space Surveillance Site (MSSS) using a 3.6 m telescope and a spatial filtering receiver that simultaneously records four star images on one camera frame. The star images were formed through pupil masks representing aperture diameters of 0.1 m, 0.5m, 1.5 m, and 3.6 m. Because each aperture is a spatial filter with a cut-off frequency inverse proportional to the aperture diameter, by estimating temporal and spatial statistics of the image centroid for different aperture diameters, one can obtain information about the spatial structure of turbulence. For each data set, we determined the camera orientation by moving the telescope at a given angle in azimuth and elevation, estimated the horizontal and vertical components of the image centroid, and evaluated the statistics of the horizontal and vertical wavefront tilt as a function of the aperture diameter and seeing conditions. We found several evidences of anisotropy of turbulence at MSSS. On four nights we observed that the variance of on-axis horizontal tilt exceeded the variance of the vertical tilt by a factor of 1.3-3.3. In addition, in several data sets the horizontal image spot diameter of the long-exposure star image exceeded the vertical image spot diameter. We also found that the mean anisotropy coefficient increases with aperture diameter, and large apertures are more likely to have higher anisotropy coefficient values than small apertures. In the case of isotropic turbulence, the power spectral densities (PSDs) of wavefront tilt are consistent with theoretical models. The telescope vibration modes were observed at 20 Hz. In the case of anisotropic turbulence, the PSDs of the horizontal tilt component have lower slope in the high frequency range, and difference between PSDs for large and small apertures is reduced. The anisotropy of turbulence and atmospheric tilt may affect the design and performance analysis of both active and passive optical systems.

Keywords: turbulence, spatial structure, anisotropy, image centroid, tilt statistics, turbulence outer scale, point spread function, power spectral density

1. INTRODUCTION

The Kolmogorov model is commonly used in theoretical studies of optical wave propagation through turbulence [1-3]. In the past decade there has been increasing experimental evidence supporting the von Karman model with a finite turbulence outer scale [4, 5]. Recently, experimental evidences of further departures from the Kolmogorov and von Karman turbulence models have been reported [6, 7]. These evidences revealed that the statistics of wavefront tilt, as well as of large scale turbulence, are anisotropic with the horizontal turbulence outer scale exceeding the vertical scale.

In this study we experimentally investigated the spatial structure of turbulence at Maui Space Surveillance Site (MSSS) using a 3.6 m telescope. We designed and built a spatial filtering receiver that measures the image centroids, or full aperture tilts, simultaneously with four aperture masks representing aperture diameters of 0.1 m,

0.5m, 1.5 m, and 3.6 m. Each aperture mask is a special filter with a cut-off frequency that is inversely proportional to the aperture diameter, $\kappa_c \sim D^{-1}$. The latter is because only turbulent inhomogeneities and wavefront aberrations on the scale of $l \geq D$ can contribute to the image centroid. By estimating temporal and spatial statistics of the image centroid, or wavefront tilt, for aperture masks representing four different aperture diameters, one can obtain information about the spatial structure of turbulence. The statistical moments of the wavefront tilt are expressed through the integral from the turbulence power spectrum with four cut-off frequencies, $\kappa_{ci} \sim D_i^{-1}$, where $I = 1,\ldots,4$. During 6 nights of imagery data collection at MSSS, fifty five data sets were recorded along with supporting data for camera orientation. The data was stored on a hard disc and then processed.

2. EXPERIMENTAL SETUP, DATA COLLECTION, AND DATA PROCESSING

An experimental study of the spatial structure of turbulence was conducted at MSSS in October, 2004 and February, 2005 using a 3.6 m telescope and specially designed and built spatial filtering receiver (SFR). The SFR uses beamsplitters and mirrors to simultaneously form four star images on one camera frame. The images are formed through pupil masks representing aperture diameters of 0.1 m, 0.5 m, 1.5 m, and 3.6 m. A small amount of tilt separates stellar images through the different apertures onto 4 quadrants of SciMeasure CCD camera. Coating on the beamsplitters and mirrors equalize the intensity in each path. The images were recorded using SciMeasure CCD operating in the 600-700 nm spectral waveband. Figure 1 shows a breadboard layout and picture of the laboratory setup.

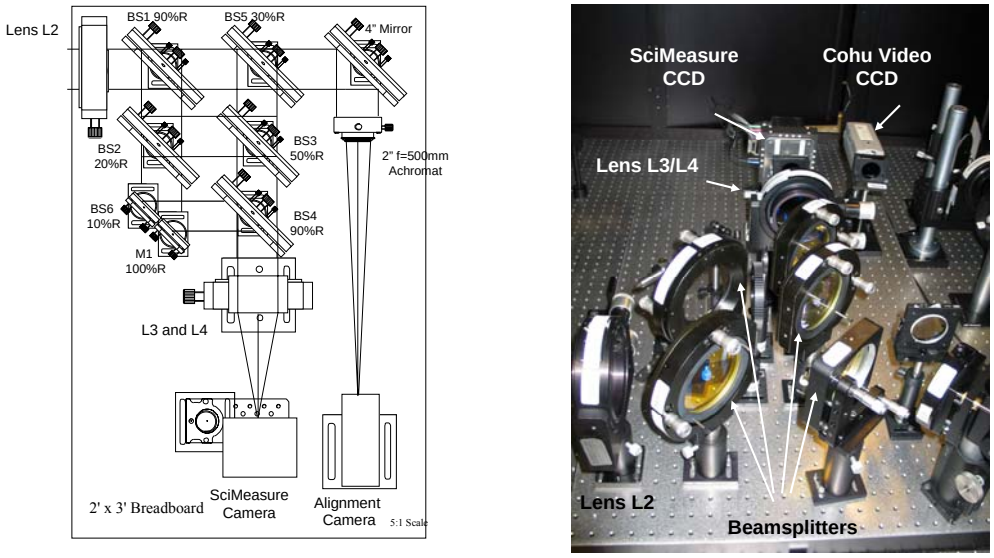

a) b)

Fig.1. Breadboard layout (a) and picture (b) of the laboratory setup in which beamsplitters separate collimated beams to form 3 pupil images. Aperture 3.6 and 1.5 m are placed in two paths. Apertures 0.5 and 0.1 m are placed together at the other pupil image. All paths are recombined at beamsplitters BS3 and BS4. Cohu video alignment camera is added to breadboard.

The camera system made by SciMeasure Analytical Systems consists of a camera head, camera controller, frame grabber, and power supply. The camera head contains a Marconi CCD39-1-1-931 frame transfer CCD sensor in a peltier package with an AR coated (Astronomy Broadband) window to isolate the chip from the thermal environment and provide for cooling. The CCD has a small format size of 80x80 pixels and is read out through four separate output ports located at the corners of the array. Thus, each quadrant of the CCD can be adjusted in offset and gain to compensate for slight variations between the separate readout amplifier circuits. The pixel size is 24 micron square for the CCD resulting in a physical size of 1.92 mm square for the active region of the array. The optical relay lenses in front of the array result in an IFOV of 0.43 arcsec, or 2.2 μrad, per pixel. The star image for each aperture was formed in a 40x40 pixel quadrant of the CCD. Each 40x40 quadrant thus has a total FOV of 17.2 arcsec, 88 μrad.

The performance of the SciMeasure camera was tested in our facility prior to field collection of the stellar images. The CCD can operate under a number of modes that produce different pixel readout rates and region-of-interest frame sizes. We acquired our stellar images using "Program 2" which resulted in a pixel read rate from each output port of 600 kpix/sec. This resulted in a frame rate of 286 fps for the full 80x80 pixel array. At the readout rate of 600 kpix/sec used to acquire stellar images, the average readout noise for the camera was 6.8 electrons rms.

The camera controller provides a number of modules in an enclosure similar to a CompactPCI that controls the operation of the CCD and transmits data to data acquisition devices. The camera data consists of a stream of 16-bit parallel pixel data in an AIA format over standard SCSI cables. This stream is input into an EDT frame grabber that mounts in a PCI slot in a standard PC type computer. The frame grabber is the PCI DV model. A separate power supply module supports the controller.

Two software packages are used with the camera and are installed on the PC used for camera control. One is made by EDT and controls the operation of the frame grabber. The application, "PDV Show", also controls the camera by transmitting control information to the camera controller through the same cable that receives the pixel data. Custom configuration files are provided by SciMeasure for use with the EDT software. A second application, "Little Joe" is also provided by SciMeasure. This program uses the EDT frame grabber interface and provides a more user friendly access to low level controls such as background level and integration time than does PDV Show.

A number of camera configurations were provided for the SciMeasure camera. These determine the frame size and readout rate obtained. These modes can be selected using the PRG or RCL commands recognized by the camera controller. These commands can be sent to the controller using PDV Show along with the program number from the table above. These modes are programmed by uploading configuration files provided by SciMeasure through the Little Joe application. The quantum efficiency was also measured and found to be 83% at a wavelength of 600 nm.

The telescope was operated in its normal sidereal pointing mode. During six nights, fifty five data sets of short-exposure images of bright stars at different elevation angles and different azimuths were recorded. The star brightness varies from 1.6 to 3 in magnitude. The data were acquired at frame rates of 100 Hz and 285 Hz. The exposure time was 10 msec for the data sets recorded at 100 Hz and 3.5 msec for the data sets recorded at 285 Hz.

Each data set included from 5,000 to 25,000 data frames. The camera orientation was determined for each data set by moving the telescope at a given angle in azimuth and elevation. The meteorological information was also recorded. We estimated the atmospheric coherence diameter, or Fried parameter, r_0, that characterizes the seeing conditions along the line of sight from the imagery data. We employed two approaches: a) we estimated r_0 from the rms image centroid for the aperture D=0.1m, and b) we estimated r_0 from the half width of half maximum (HWHM) of the long-exposure point spread function (PSF) obtained by averaging multiple short-exposure frames.

Based on the camera orientation data, all images in the data set were rotated so that the horizontal pixel row in each frame corresponded to the azimuth direction. The image processing procedure was similar to that used in [6 and 7]. This includes a sky background subtraction and flat field correction. From the imagery data, the horizontal and vertical components of the image centroid were then calculated and long-exposure PSFs were determined. The tilt statistics were estimated, and the outer scale and Fried parameter were determined. The power spectral densities of the image centroid were found.

3. EXPERIMENTAL EVIDENCE OF ANISTROPY OF TURBULENCE

The time series of the horizontal and vertical image centroid, or wavefront tilt, for a 3.6 m aperture diameter for two data sets recorded on February 15th and February 17th are shown in Figure 2. Note that the rms for the horizontal and vertical centroid for the February 15th data set in Figure 2a are approximately equal, whereas the rms of the horizontal centroid exceeds that for the vertical centroid by a factor of 3.3 for the February 17th data set in Figure 2b. This implies that the anisotropy coefficient defined as the ratio of the rms of the horizontal tilt to the rms of the vertical tilt, $\alpha = \sigma_{Az} / \sigma_{El}$, is equal to $\alpha = 0.96$ in the first data set, and $\alpha = 3.33$ in the second data set. These estimates of the anisotropy coefficients were obtained using the first 5,000 frames in the data set. The data shown in Fig. 2b provide direct evidence of anisotropy of an atmospheric tilt.

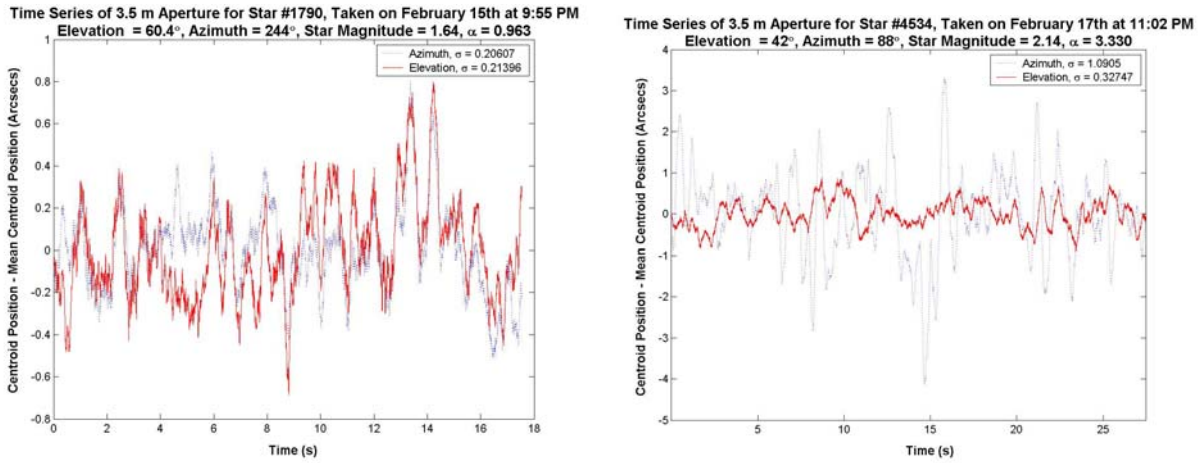

a) b)

Fig. 2. A time series of the horizontal (marked azimuth) and vertical (marked elevation) image centroid in the case of (a) isotropic ($\alpha = 0.96$) and (b) anisotropic ($\alpha = 3.3$) turbulence. The brightness of the star #1790 is 1.64 in magnitude, and the brightness of star # 4334 is 2.1. The rms of the horizontal tilt exceeds the rms of the vertical tilt by a factor of 3.3

Figure 3 shows the dependency of the rms image centroid, or wavefront tilt, on the aperture diameter measured on two nights. Note that in the isotropic case in Figure 3a, where $\alpha = 0.96$, the rms of the horizontal and vertical tilt components are comparable. However, for the anisotropic case in Figure 3b, where $\alpha = 3.33$, , the rms of the horizontal tilt significantly exceeds that of the vertical tilt. The difference between the rms of horizontal and vertical tilts increases with the aperture diameter.

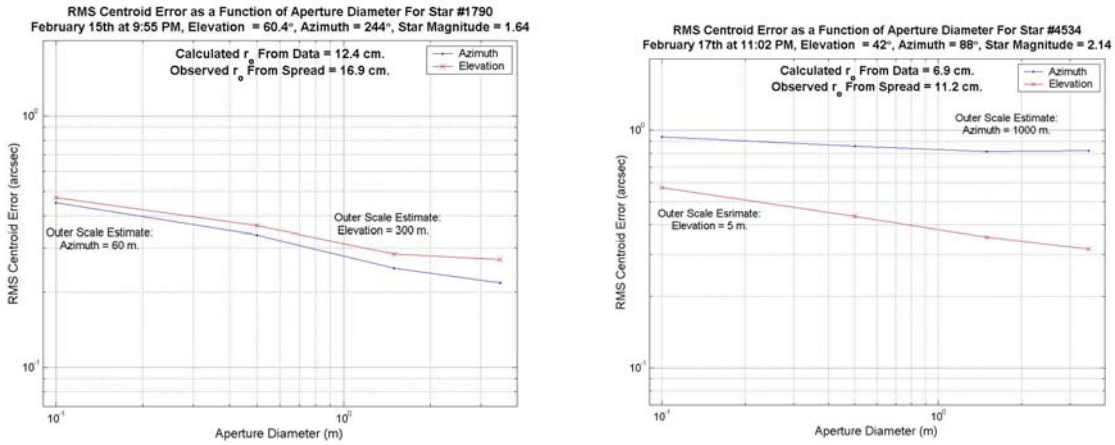

a) b)

Fig. 3. Dependence of the rms of the horizontal and vertical tilt on the aperture diameter for (a) isotropic and (b) anisotropic turbulence.

Figure 4 depicts the long-exposure images of two stars recorded using the 3.6 m aperture diameter mask on February 15th and February 17th. The long-exposure images were obtained by summing up 5000 frames in the corresponding data sets. Note that the long-exposure star image in Figure 4a, or long-exposure PSF, is isotropic, which is consistent with prediction of conventional imaging theory.[8,9] However, the long-exposure PSF in Figure 4b is strongly anisotropic. The image spot diameter in the horizontal direction exceeds the spot diameter in the vertical direction by a factor of 2.14. This provides further experimental evidence of anisotropy of turbulence.

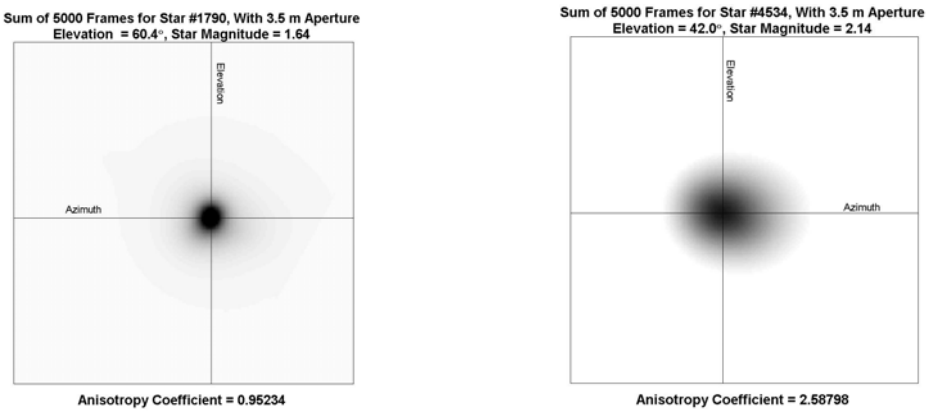

a) b)

Fig. 4. A long-exposure point spread function obtained by averaging 5,000 short-exposure images in the case of (a) isotropic and (b) anisotropic turbulence.

4. STATISTICS OF ANISTROPY COEEFICENT AND COHERENCE DIAMETER

Figure 5 shows the dependence of the anisotropy coefficient on the zenith angle measured on six nights. On four nights, February 15, 16, and 18, 2005 and October 28, 2004, the anisotropy coefficient was greater than $\alpha = 1$. On three nights the anisotropy coefficient increased with the zenith angle, which is consistent with the notion that anisotropy of turbulence is the strongest near the ground. On the night of February 18, 2005, the anisotropy coefficient decreased with the zenith angle. Note that on this night, the seeing condition characterized by the Fried parameter was the worst (see Figure 6). Specifically, the r_0 values corrected to the 500 nm wavelength and at the zenith were lees than or equal to 10 cm, whereas on February 15 and 16, 2005 the mean r_0 values were 14 cm and 12 cm, respectively.

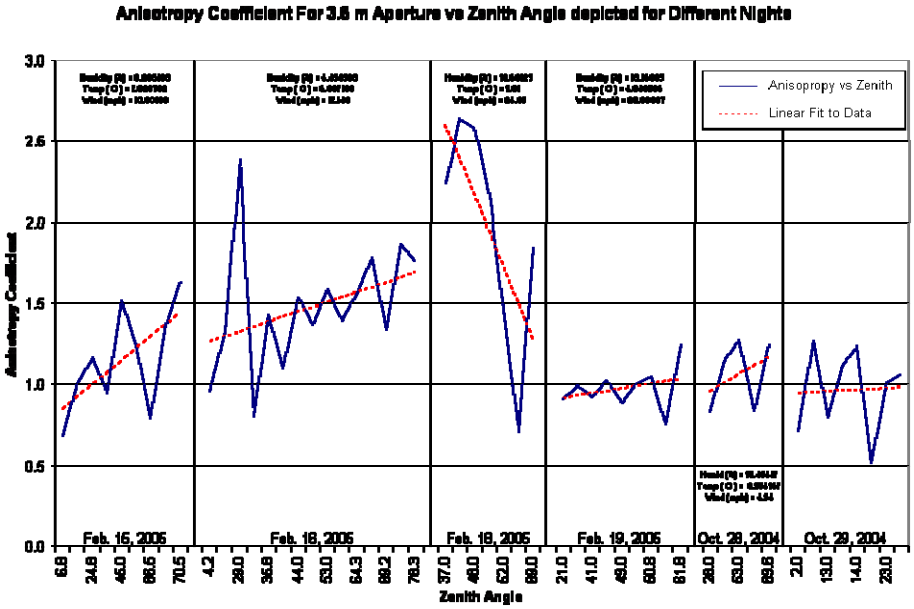

Fig.5. Anisotropy coefficient versus zenith angle measured on six nights at MSSS.

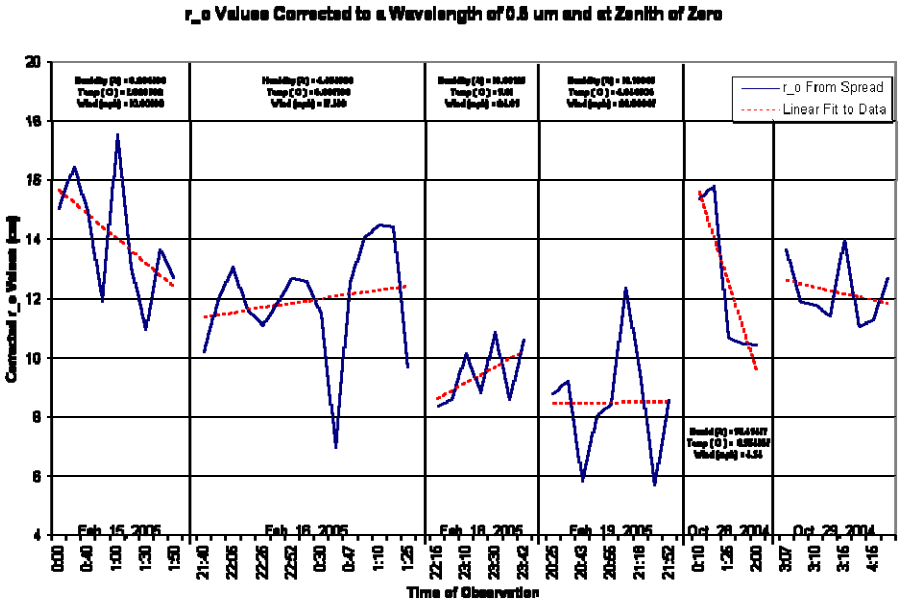

Fig. 6. Coherence diameter versus observation time measured during six nights at MSSS.

Figure 7a depicts the dependence of the mean anisotropy coefficient calculated for all data sets on the aperture diameter. The anisotropy coefficient increases rapidly with the aperture diameter when $D \leq 0.5$m. For $D \geq 1.5$ m, the curve has a linear slope. Figure 7b shows the probability distribution of the anisotropy coefficient for different aperture diameters calculated for all data sets. Note that the probability of the anisotropy coefficient strongly depends on the aperture diameter. The larger the aperture diameter, the greater the probability of obtaining high values for the anisotropy coefficient. For $D = 0.1$ m, the probability of $\alpha = 1$ is 55%, and the probability of $\alpha > 1.75$ is zero. For $D = 3.5$ m, the probability of $\alpha = 1$ is about 20%, whereas the probability of $\alpha > 2$ and $\alpha > 2.75$ is 10% and 5%, respectively. Both the dependence of the anisotropy coefficient on the aperture diameter (Figure 7a) and the dependence of the probability distribution of the anisotropy coefficient on aperture diameter (Figure 7b) can be explained by the following: when large scale turbulence becomes anisotropic, small scale turbulence remains isotropic. Increasing the aperture diameter increases the contribution of isotropic small-scale turbulence to the image centroid due to spatial filtering properties of the pupil mask.

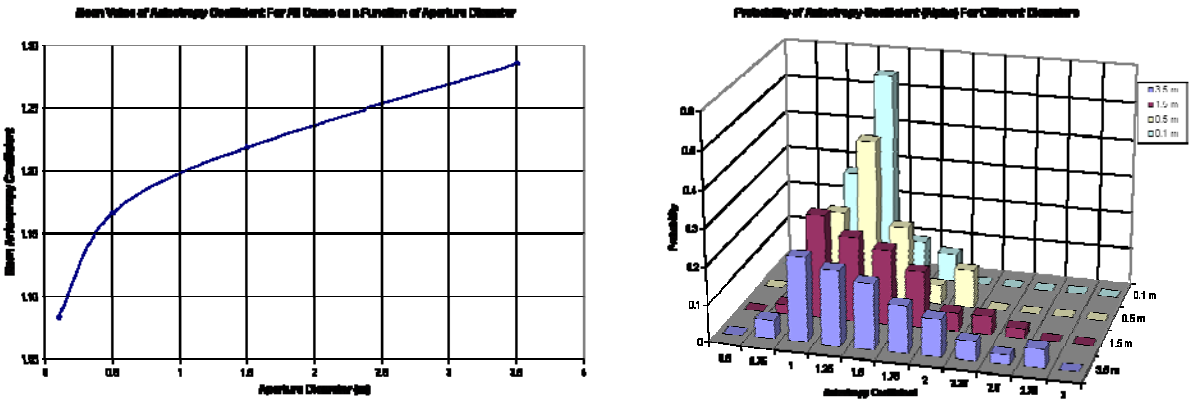

a) b)

Fig. 7 (a) Dependence of the anisotropy coefficient on the aperture diameter and (b) dependence of probability distribution of anisotropy coefficient on the aperture diameter.

Figure 8 shows a correlation plot of the anisotropy coefficient versus corrected atmospheric coherence diameter for the data set recorded on February 18, 2005. The solid curve was calculated using all data points. The dashed curve

was calculated when the "outlier" that corresponds to the value of $\alpha = 0.65$ was rejected. In both cases, the correlation between anisotropy coefficient and r_0 is negative – the high values of anisotropy coefficient correspond to low values of r_0. This implies that anisotropy of turbulence is higher near the ground where the turbulence is the strongest. However, when the data for all six nights were combined, no correlation between the anisotropy coefficient and atmospheric coherence diameter was observed.

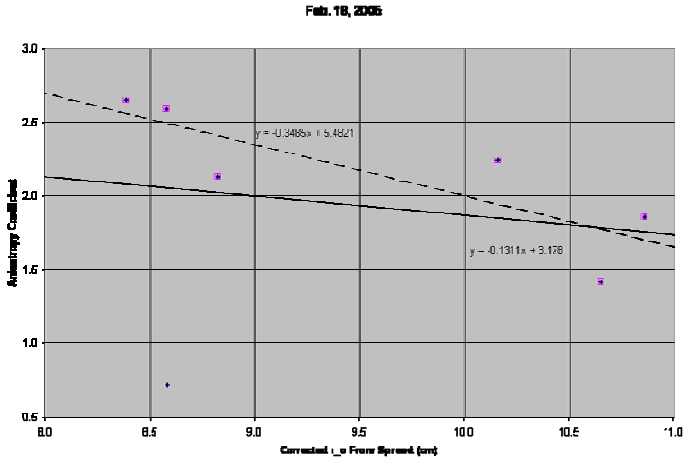

Fig. 8. Correlation of the anisotropy coefficient and corrected values of the Fried parameter for the data sets recorded on February 18, 2005.

Figure 9 compares the r_0 values determined using two different approaches: a) calculated from the rms image centroid for the aperture D = 0.1 m, and b) estimated from the half width of half maximum (HWHM) of the long-exposure point spread function (PSF). The estimates obtained by using these two approaches are consistent with each other. The slope of the correlation curve is close to one. The small bias of the correlation curve could be due to the effect of anisotropic of turbulence that has not been taken into account in conventional imaging theory.[8,9] Figure 10 depicts the probability distribution of the corrected values of the atmospheric coherence diameter.

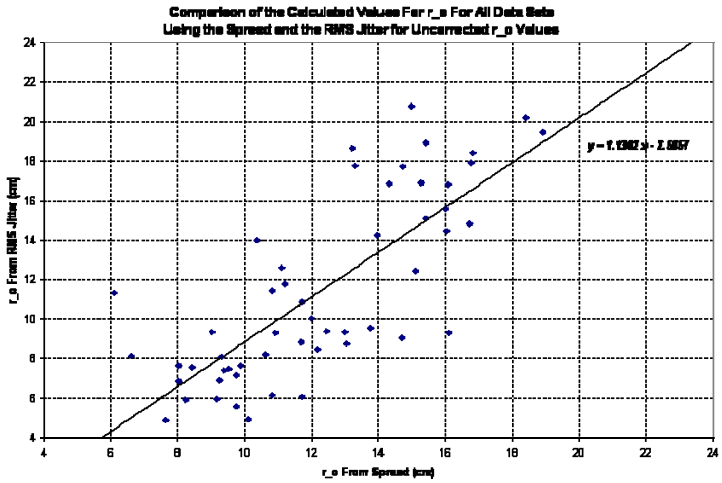

Fig. 9. Correlation of the atmospheric coherence diameter determined from the image centroid and from the HWHM of the long exposure PSF. The slope of the correlation curve is close to 1. The small bias of the correlation curve could be due to the effect of anisotropy of turbulence that has not been taken into account in the conventional imaging theory.[8]

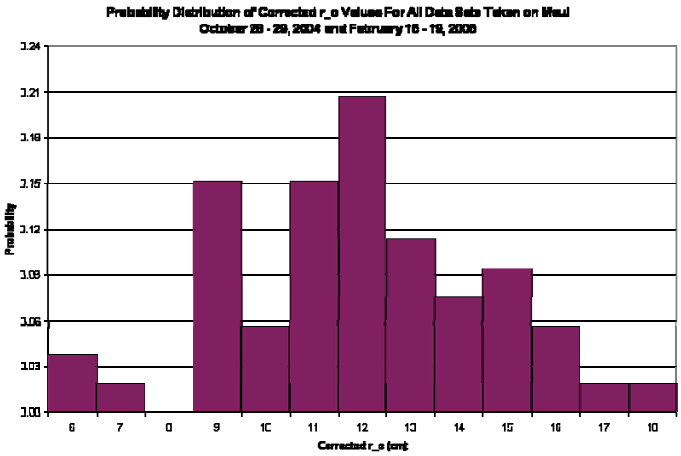

Fig. 10. Probability distribution of the corrected values of Fried parameter for all data sets recorded during six nights at MSSS.

5. DETERMINATION OF TURBULENCE OUTER SCALE

We showed that measurements of the image centroid using different aperture masks provide information about spatial structure of turbulence. It is easy to show that these measurements also provide estimates for the turbulence outer scale. The turbulence outer scale affects the slope of the dependence of rms centroid on aperture diameter shown in Figure 3.

The procedure for outer scale determination uses the same approach that was employed in [7]. The outer scale was determined using a least square fit to analytical prediction for the rms centroid versus aperture diameter calculated using the von Karman power spectrum. The horizontal and vertical turbulence outer scales were estimated independently. The calibration curves for turbulence outer scale determination were calculated using the von Karman power spectrum and an analytical expression for the rms centroid versus aperture diameter.

Figure 11 shows the probability distributions of the horizontal and vertical turbulence outer scale for all data sets obtained at MSSS. For the vertical turbulence outer scale, the most probable values are $L_0 \leq 30$ m, whereas for the horizontal outer scale, the most probable values are $L_0 \geq 300$ m. This further supports the notion of anisotropy of turbulence.

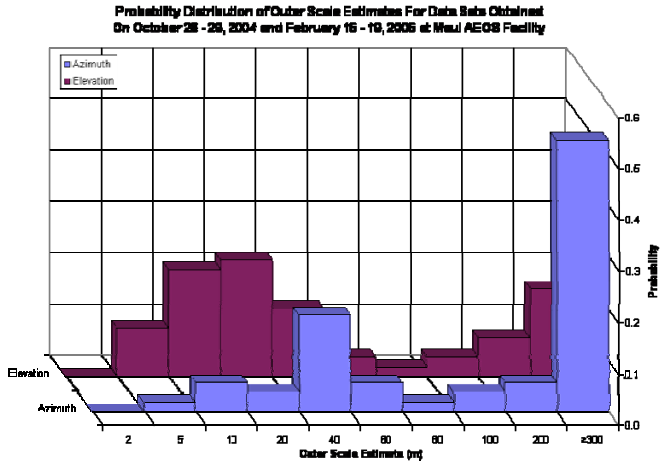

Fig. 11. Probability distribution of the horizontal and vertical turbulence outer scale for all data sets obtained at Maui Space Surveillance Site.

6. POWER SPECTRAL DENSITY

Finally, Fig.12 shows the power spectra densities (PSD) of the horizontal and vertical tilt for the aperture diameters D = 0.1 m and D = 3.5 m both for the case of isotropic turbulence (α = 0.96) and anisotropic turbulence (α = 2.1). The PSDs for isotropic turbulence (Figures 13a and b) are consistent with the theoretical dependences $f^{-2/3}$ and $f^{-11/3}$ predicted from the frozen turbulence hypotheses and the Kolmogorov model.[2] A 20 Hz vibration mode is seen in the power spectra for both horizontal and vertical tilt components. In the case of anisotropic turbulence (Figures 13c and d), the PSD for the horizontal tilt has a different shape than the PSDs for isotropic turbulence in Figures 13a and b. Also in the anisotropic turbulence cases, the separation between the PSDs for small, D = 0.1 m, and large, D = 3.5 m, apertures is reduced. The slope of the PSD for the small aperture in the high frequency range is lower.

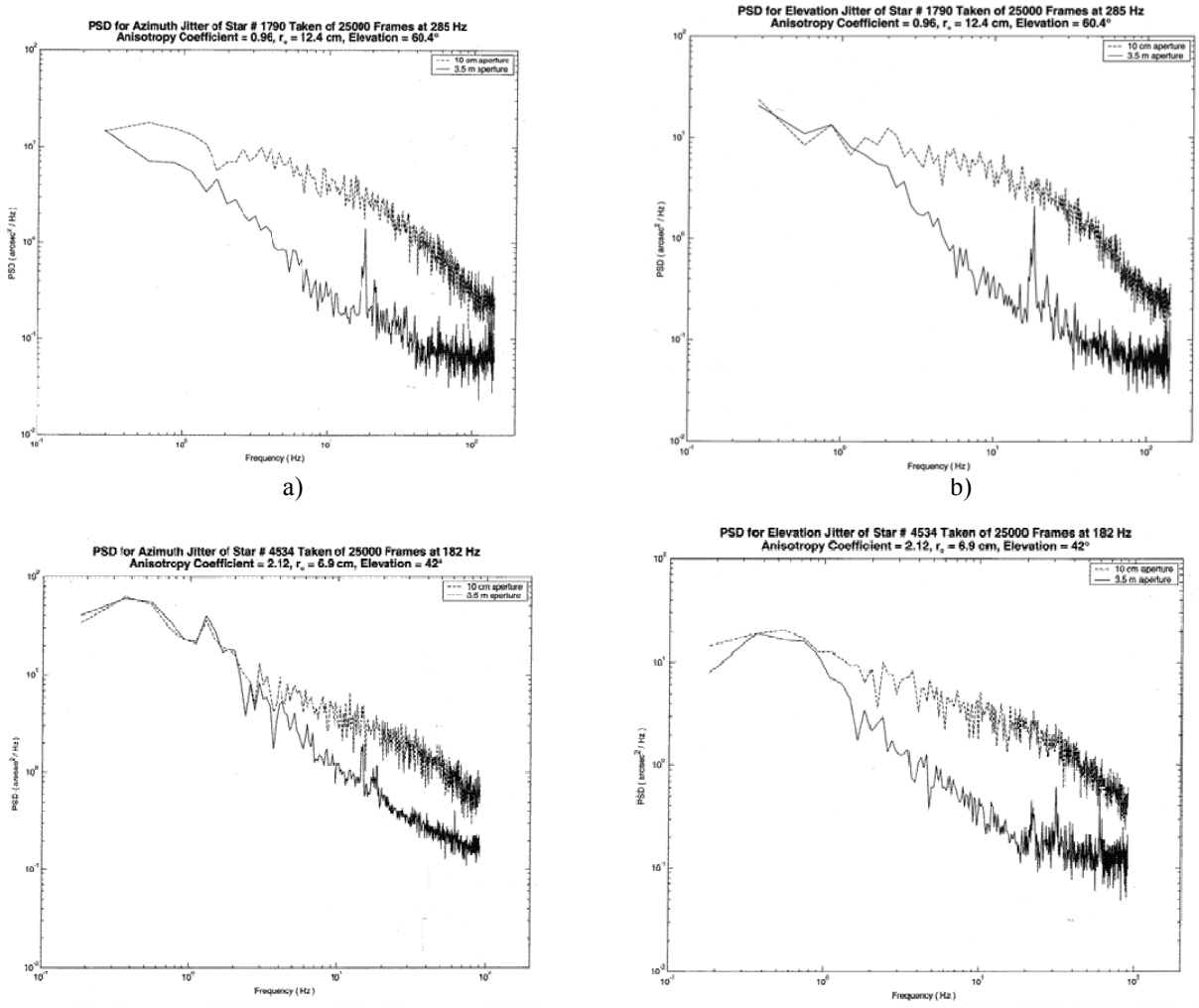

Fig. 12. Temporal power spectral densities for (a),(c) horizontal (azimuth) and (b),(d) vertical (elevation) image centroid components for aperture diameter D = 0.1 m and D = 3.5 m. The PSDs for (a),(b) isotropic turbulence and for (c), (d) anisotropic turbulence.

7. DISCUSSION AND CONCLUSIONS

This paper presents results of an experimental study of the spatial structure of turbulence at Maui Space Surveillance Site. The results can be summarized as follows:

- Anisotropy of atmospheric tilt was observed on four nights when the rms of horizontal tilt consistently exceeded the rms of vertical tilt. This provides evidence of anisotropy of turbulence;

- An anisotropy of a long-exposure PSF was observed, when the image spot diameter in the horizontal direction exceeded the spot diameter in the vertical direction;

- The mean anisotropy coefficient increases with aperture diameter. The probability of higher anisotropy coefficient values increases with increasing telescope diameter;

- The power spectral densities for isotropic turbulence generally follow the power laws expected from the Kolmogorov turbulence model;

- In the case of anisotropic turbulence, the PSDs for the horizontal tilt have different functional form. A difference between the PSDs for small and large apertures is reduced, as well as the slope of the PSD for D = 0.1 m, in the high frequency range.

Therefore the results reported in this study provide experimental evidence of anisotropy of turbulence at Maui Space Surveillance Site. The anisotropy of turbulence and atmospheric tilt may affect the design and performance analysis of both active and passive optical systems.

8. ACKNOWLEDGMENTS

This work was funded by the National Science Foundation under the Grant No. AST-0123466. The authors greatly acknowledge their support. The authors wish to express their appreciation to Mike Roggemann for stimulating discussions and technical personal and telescope operators at MSSS for help in execution of the experiments.

REFERENCES

1. Kolmogorov, A. N., The local structure of turbulence in an incompressible viscous fluid for very large Reynolds numbers, *C. R. (Doki) Acad. Sci*. U. S. S. R. Vol. 30, 301-305, 1941.

2. Tatarskii, V. I., *Wave Propagation in a Turbulent Medium*, McGraw-Hill, New York, 1961.

3. Andrews, L. and Phillips, R. L., *Laser Beam Propagation through Random Media*, SPIE Optical Engineering Press, Bellingham, 1998.

4. Ziad, A., Bongino, J., Martin, F., and Agabi, A., Experimental estimation of the spatial-coherence outer scale from a wavefront statistical analysis, Astron. and Astrophys., Vol. 282, 1021-1033, 1994.

5. Tokovinin, A. A., Ziad, A., Martin, F., Avita, R., Borgnino, J., Cohan, R., and Sarazin, M., Wavefront outer scale monitoring at La Silla, SPIE Proc., Vol. 3353, 1155-1162, 1998.

6. Belen'kii, M. S., Karis, S. J., Brown, J. M. and Fugate, R. Q., Experimental study of the effect of non-Kolmogorov turbulence on star image motion, Proc. SPIE, Vol. 3126, 113-123, 1997.

7. Belen'kii, M. S., Barchers, J. D., Karis, S. J., Osmon, C. L., Brown II J. M. and Fugate, R. Q., Preliminary experimental evidence of anisotropy of turbulence and the effect on non-Kolmogorov turbulence on wavefront tilt statistics, SPIE Proc., Vol. 3762, 396-406, 1999.

8. Fried, D. L., Optical resolution through a randomly inhomogeneous medium for very long and very short exposures, J. Opt. Soc. Am., Vol. 56, 1372-1379 (1966).

9. J. W. Goodman, *Statistical Optics*, John Wiley & Sons, NY 1985.